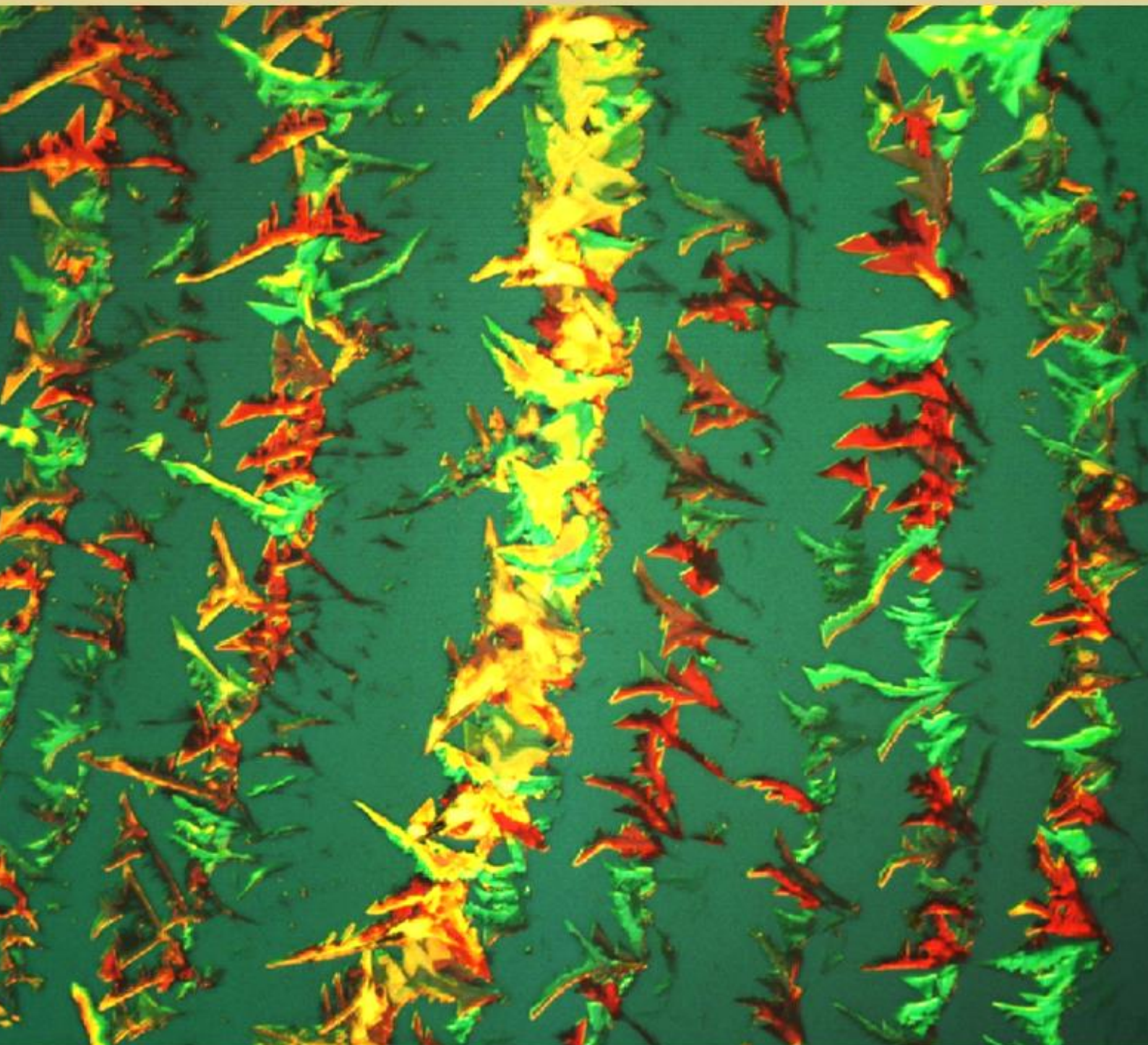


Volume 3, Number 2

December 2021

Nanomaterials Science & Engineering



Volume 3, Number 2

December 2021

Nanomaterials Science & Engineering

Title

Nanomaterials Science & Engineering (NMS&E), Vol.3, No.2, 2021

Editors-in-Chief

Igor Bdikin
Paula Alexandrina de Aguiar Pereira Marques
Duncan Paul Fagg

Editorial Board

Alexander Titov, Andrei Kovalevsky, António Manuel de Amaral Monteiro Ramos, António Manuel de Bastos Pereira, António Manuel Godinho Completo, Bagautdinov Bagautdin, Binay Kumar, Budhendra Singh, Cicero R. Cena, D. Pukazhselvan, Dmitry A. Kiselev, Dmitry Karpinsky, Eudes Borges de Araujo, Gil Gonçalves, Gonzalo Guillermo Otero Irurueta, Indrani Coondoo, João Paulo Davim Tavares da Silva, José Coutinho, Maciej Wojtas, Manoj Kumar Singh, Margarida Isabel Cabrita Marques Coelho, Maxim Silibin, Münir Tasdemir, Neeraj Panwar, Nikolai Sobolev, Oleksandr Tkach, Paula Celeste da Silva Ferreira, Philip Leduc, Radheshyam Rai, Sergey Bozhko, Svitlana Kopyl, Vincent Ball, Vítor António Ferreira da Costa, Vladimir Bystrov, Yuri Dekhtyar

Editorial Managers

Igor Bdikin
Gil Gonçalves
Raul Simões

Cover and Logo

Igor Bdikin (Thymine microcrystals, Optical image with crossed polarizers, 1.0x0.8 mm², x100)

Publisher

University of Aveiro

Support

Serviços de Biblioteca, Informação Documental e Museologia
Centre for Mechanical Technology & Automation (TEMA)
Mechanical Engineering Department
University of Aveiro

Copyright Information

All work licensed under Creative Commons Attribution License that allows others to share the work with an acknowledgement of the work's authorship and initial publication in this journal. Copyrights to illustrations published in the journal remain with their current copyright holders. It is the author's responsibility to obtain permission to quote from copyright sources.

Mailing Address

Department of Mechanical Engineering
University of Aveiro
Aveiro 3810-193
Portugal
E-mail: bdikin@ua.pt

ISSN: 2184-7002

S. Shanmuga Sundari, S. Karthika, A. Durairajan, M.P.F. Graça, M.A. Valente YAG:Ag nanophosphors – synthesis and characterization	35-42
S.M. Mikhalev, Paulo S.B. Julião, F.J.A. Loureiro, A.L. Shaula, D.P. Fagg Antimony-lead melts for high temperature electrochemical applications	43-46
Chandra Shekhar Maurya, Chiranjit Sarkar Magnetic Field, Heat Transfer and Rheological Analysis of a agnetorheometer using Finite Element Method	47-53

YAG:Ag nanophosphors – synthesis and characterization

S. Shanmuga Sundari^{1,*}, S. Karthika¹, A. Durairajan², M.P.F. Graça², M.A. Valente²

¹ Department of Physics, PSGR Krishnammal College for Women, Coimbatore, 641004, India

² I3N-Aveiro, Department of Physics, University of Aveiro, Aveiro 3810 193, Portugal

* Corresponding author, e-mail address: shanmugi.s@gmail.com

Received 14 October 2021; accepted 14 December 2021; published online 30 December 2021

ABSTRACT

Yttrium Aluminium Garnet ($Y_3Al_5O_{12}$)-YAG and Silver (Ag) of four different mol% in YAG (0.5, 1.0, 1.5 and 2.0 mol % of Ag) – YAG:Ag were synthesized by Pechini method. The synthesized pure YAG was white in colour but the incorporation of Ag in the YAG matrix forms colour centre and turns to pink. The intensity of pink Ag doped YAG is increasing with the increase in mol% of Ag. In the present work the synthesis and the preliminary characteristics about the structure, morphology, elemental composition and optical properties were studied using X-ray diffraction (XRD), Fourier Transform Infrared (FTIR), Scanning Electron Microscopy-Energy Dispersive Spectroscopy (SEM – EDAX), Ultraviolet-visible spectroscopy (UV-Vis) and Photoluminescence spectroscopy (PL). The sharp peak in the XRD reveals the good crystalline nature of the samples. The bending and stretching vibrations of the oxygen groups associated with YAG was observed in FTIR spectra. Tube like morphology was noticed in the SEM and increase in crystallite size is also perceived in YAG:Ag. The elemental mapping by EDAX confirmed the purity of synthesised samples. UV spectra shows the absorption peaks due to Ag incorporated in the YAG matrix. The PL spectra reveals the blue and green light emitting properties of the synthesized YAG nanophosphors.

1. INTRODUCTION

Research and development of nanophosphors is a part of rapidly growing nanoscience and nanotechnology. YAG-based nanophosphors have drawn significant interest due to their excellent luminescence property, high physical stability and low synthesis cost. Doping of the rare earth metals into the host matrix demonstrate an approach to develop highly efficient and stable nanophosphors for light and display devices. Especially these phosphors have applicability in the field of colour television display, flat panel display, plasma display panels, device indicators, automobile, headlights, etc. and hence they are emerging as an important class of the optical materials [1].

Recently, S.A. Hassanzadeh-Tabrizi *et al* [2] reported cerium-doped yttrium aluminium garnet (YAG:Ce) powder that were synthesized by Pechini method. They observed pure YAG phase only after

800 °C and the average size of the particles was about 70 nm. The photoluminescence spectrum of the crystalline YAG:Ce phosphors showed the green-yellow emission with 5d→4f transition as the most prominent group. Similarly green phosphor $Y_3Ga_5O_{12}: Tb$ (YGG) was synthesized by Nanfei Zhua *et al* [3]. The excitation spectrum is dominated by the 4f→5d transition of Tb^{3+} at 263 nm. The strong emission peaks for the heavily doped phosphors are observed at 489 and 543 nm. V. Tucureanu *et al* [4] reported that cerium doped yttrium aluminium garnet (YAG:Ce) phosphors prepared by solid-state reaction method, particularly the sol gel and (co) precipitation methods. In addition to that the effect of co-doping with rare earth elements and the corresponding red/blue shift in the spectrum was explained in detail. It was seen that the transition from the amorphous phase to the crystalline phase appears at 800 °C. Similarly Manisha Upasani *et al* [5] synthesized Magnesium (Mg) co-doped YAG:Ce

phosphors by single step combustion method by mixed fuel at 500 °C. The doping effect of Mg on the luminescence intensity of YAG:Ce was studied and the results showed that the luminescence intensity decreases significantly with the increase of Mg concentration. Three polycrystalline powders of Y–Al–O compounds, $Y_3Al_5O_{12}$ (YAG), $YAlO_3$ (YAP), $Y_4Al_2O_9$ (YAM) were reported by *Masaaki Harada et al* [6]. It was noted that all the compounds were obtained in a single phase. Thermal analysis showed that the crystallization temperatures were 900 °C for YAG and YAM, and 1100 °C for YAP, which was 300 °C lower than that of sol–gel process and also reported the phase change of each compound with temperature. *Case Collins Reza T et al* [7] studied the excellent luminescence performance of yttrium aluminium garnet ($Y_3Al_5O_{12}$) phosphors as a function of Chromium (Cr^{3+}) concentration.

Yttrium aluminium garnet can be a useful matrix to dope certain rare earth elements to enhance the luminescent property of YAG. This paper reports the preparation of pure Yttrium Aluminium Garnet ($Y_3Al_5O_{12}$)-YAG and YAG:Ag by Pechini method. This may lead to differences in their optical and luminescent properties. The synthesized pure YAG was white in colour but the incorporation of Ag in the YAG matrix forms colour centre and turns to pink. The intensity of the pink is increasing with the

increasing mol% of Ag. In the present work the synthesis and the preliminary characteristics about the structure, morphology, elemental composition and optical properties were studied using X-ray diffraction (XRD), Fourier Transform Infrared (FTIR), Scanning Electron Microscopy-Energy Dispersive Spectroscopy (SEM – EDAX), Ultraviolet–visible spectroscopy (UV-Vis) and Photoluminescence spectroscopy (PL).

2. EXPERIMENTAL DETAILS

Yttrium nitrate $Y(NO_3)_3 \cdot 6H_2O$, aluminium nitrate $(Al(NO_3)_3 \cdot 9H_2O)$ silver nitrate ($AgNO_3$) citric acid ($C_6H_8O_7$), ethylene glycol ($C_2H_6O_2$) and distilled water (H_2O) of high purity (99.99%) from sigma aldrich were used for the synthesis. Yttrium Aluminium Garnet ($Y_3Al_5O_{12}$) was synthesized by Pechini method which involves stirring, drying and calcination. Pure $Al(NO_3)_3 \cdot 9H_2O$, $Y(NO_3)_3 \cdot 6H_2O$ were used as cation source. These nitrate salts that behaves as anion were dissolved in 80 ml of distilled water and citric acid at the ratio of 1:2. These metal salts were dissolved at molar ratio, Y: Al of 3:5 respectively. This mixture was stirred until a clear solution was obtained. Ethylene glycol which acts as a polymerization agent was added into the solution. The solution was continuously stirred at 80 °C until the gel was formed. After the

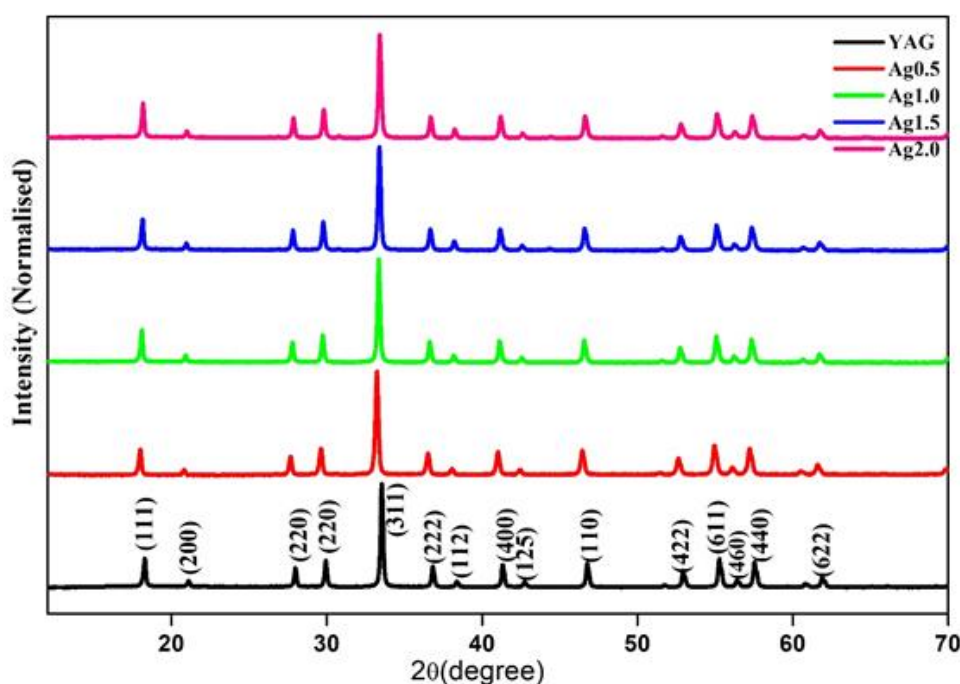


Figure 1. XRD pattern of YAG and doped YAG.

gelation, the gel was dried in oven at 100 °C for 18 h. Then preheated for 4 h at 600 °C. This powder was crushed and fired at 1200 °C for 4 h and pure yttrium aluminium garnet nano powder was obtained. In the case of Ag doped-Y₃Al₅O₁₂, silver was added in 0.5, 1.0, 1.5 and 2.0 mol % with the cation source and stirred in 80 ml of distilled water. Similar procedure of YAG was followed to synthesis Ag doped YAG. In this work, Ag0.5, Ag1.0, Ag1.5 and Ag2.0 represents the 0.5, 1.0, 1.5 and 2.0 mol % of Ag in YAG matrix respectively. X-ray diffractometer (Model Panalytical) was employed using Cu-K_α radiation source operating at 45 kV and 40 mA. Radial scans were recorded) from 10° to 70°. FTIR spectra of YAG and Ag doped YAG nano particles was observed by FTIR spectrometer (Model: Nicolet 6700) having scan range from 400 to 4000 cm⁻¹. The spectra were observed in total reflectance mode at scanning rate of 8 cm⁻¹. Field emission gun scanning electron microscope (FEG-SEM) sigma-3 was used to investigate morphology of nanoparticles while energy dispersive spectroscopic analysis was performed by Oxford EDS detector coupled with FESEM (MIRA Tescan 3) at 20 keV energy for elemental analysis. The UV-visible absorption spectra of pure YAG and Ag doped YAG were recorded using V-670 spectrophotometer (double beam instrument) from 400 to 800 nm. Spectrofluorophotometer - Shimadzu RF-5301PC series is used to investigate the

photoluminescence property of synthesised nano particles.

3. RESULTS AND DISCUSSION

3.1. Structural Properties

3.1.1. X-ray Diffraction (XRD)

X-ray diffraction (XRD) was performed to identify the crystalline phases in the synthesized nano phosphor powder. The XRD pattern is shown in figure 1. The sharp and well-defined peaks indicate the perfect crystalline nature of the YAG and Ag doped samples. The recorded pattern is well matched with the reported results of YAG phase (JCPDS: 33-0040). There is no sign of any impurity phase formation like yttrium aluminium perovskite and yttrium aluminium monoclinic. This result indicates that 1200 °C is the exact temperature to synthesis YAG materials. The addition of Ag in YAG does not show major changes in the XRD peaks except a slight shift towards a lower angle side. This suggests that there is expansion of YAG matrix after the addition of Ag.

Scherer's equation was used to calculate the crystallite mean size (D), [8]

$$D = \frac{k\lambda}{\beta \cos\theta} \quad (1)$$

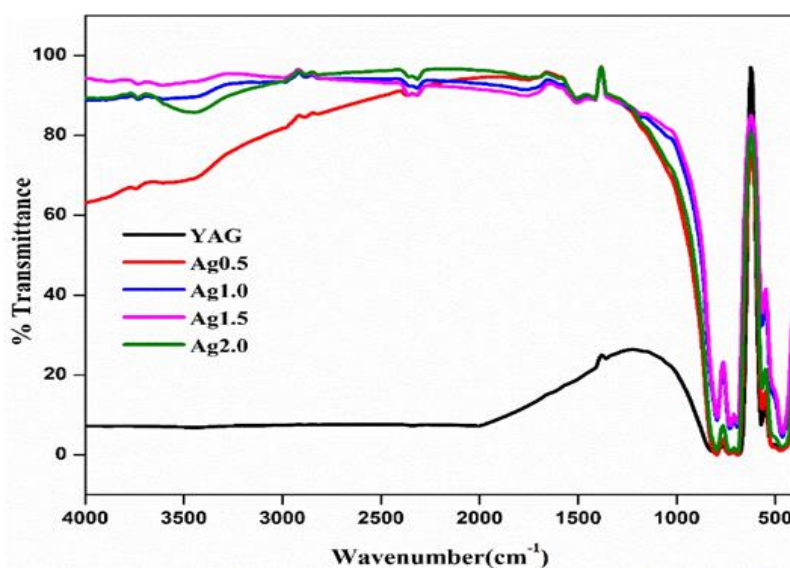


Figure 2. FTIR spectra of YAG and Ag doped YAG.

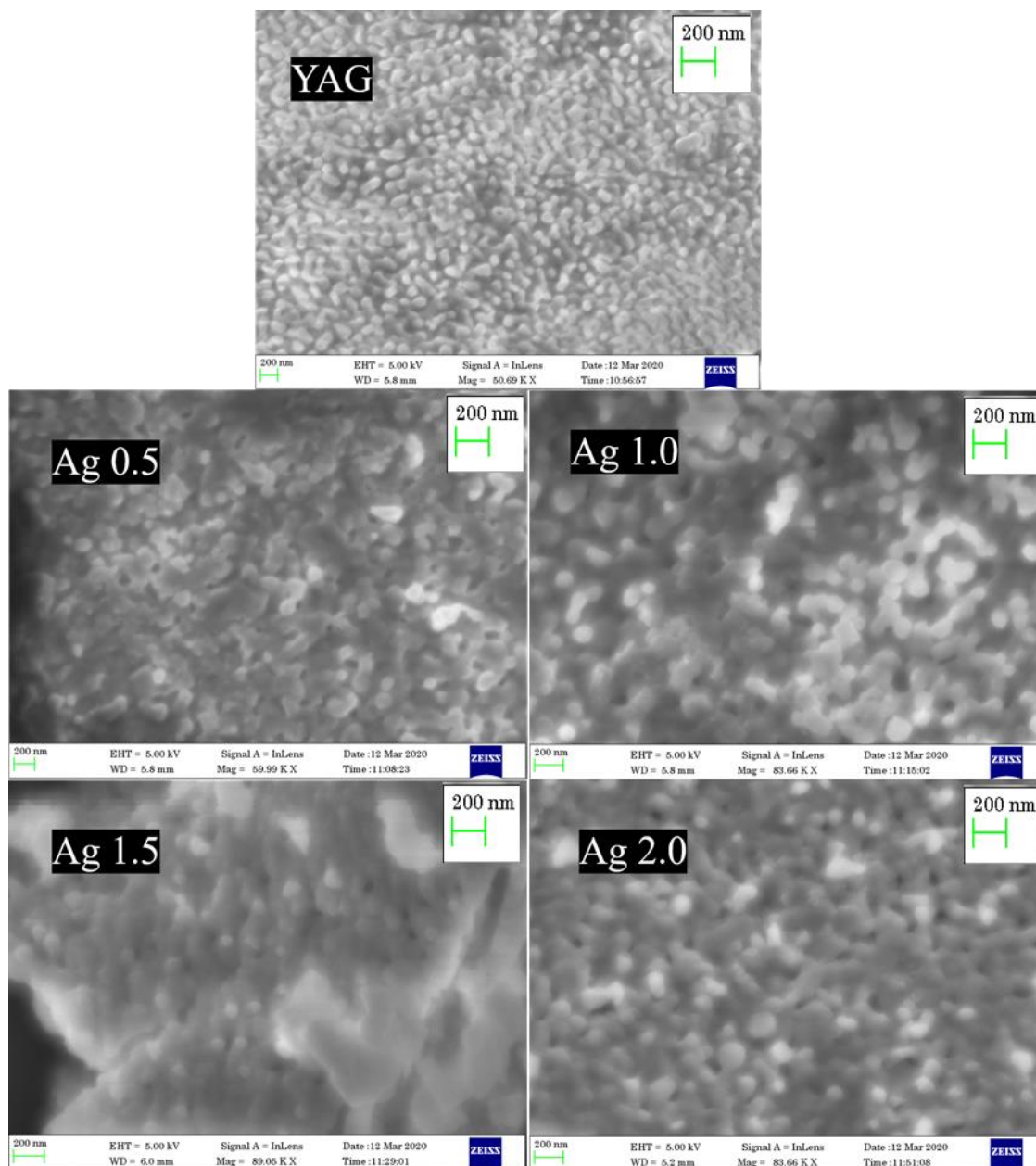


Figure 3. SEM micrograph of YAG and Ag doped YAG.

where k is dimensionless shape factor, λ (1.5418 Å) is x-ray wavelength and β is the line broadening at full width at half maximum of diffraction peak intensity. The crystallite mean size was calculated

for all the samples using major intense diffraction peaks, resulting to 81nm for YAG. Whereas mean values of crystallite size calculated for the Ag doped YAG samples were 83 nm, 96 nm, 106 nm

Table 1. Elemental mapping results.

Element	Weight%	Atomic%	Element	Weight%	Atomic%
YAG			Ag 1.5		
O K	35.50	63.71	C K	36.44	56.29
Al K	20.88	22.21	O K	26.07	30.23
Y L	43.62	14.08	Al K	11.83	8.13
			Y L	25.17	5.26
			Ag L	0.50	0.09
Total	100.00	100.00	Total	100.00	100.00

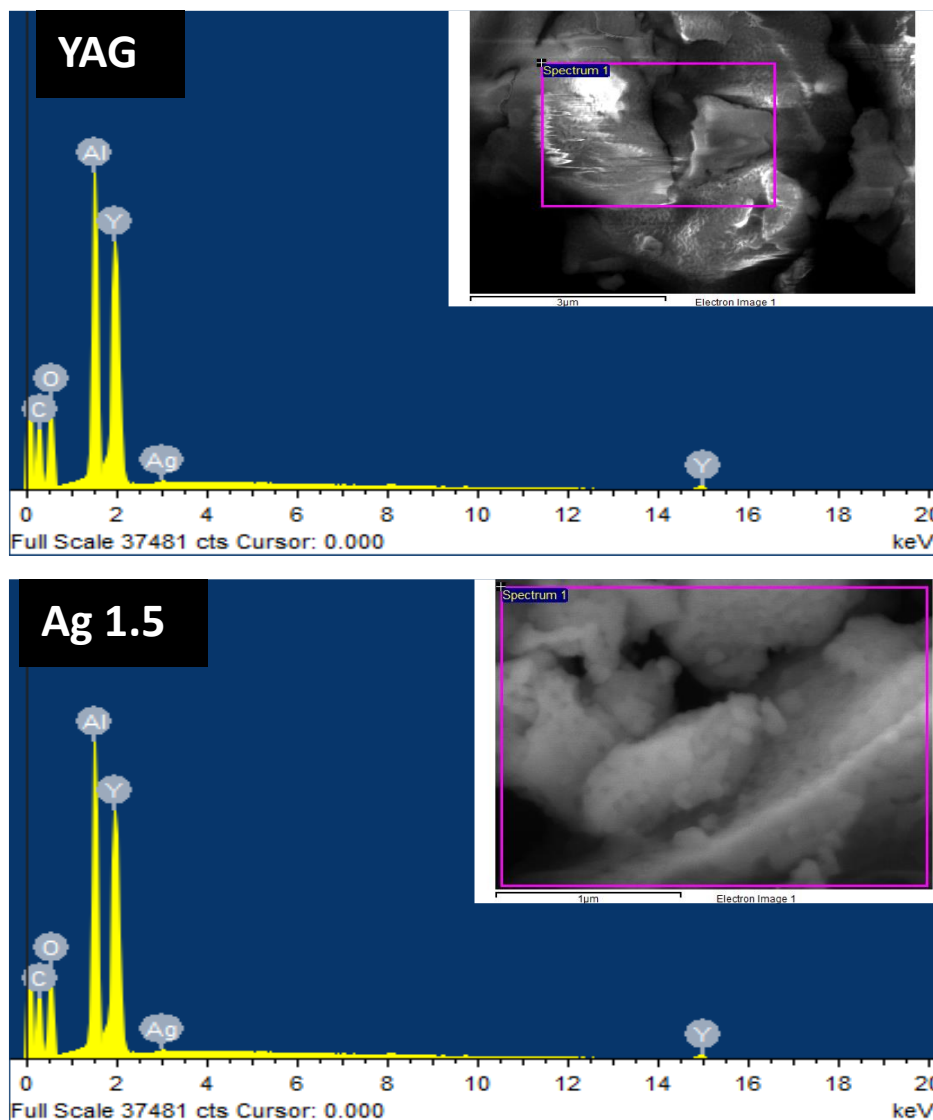


Figure 4. Elemental mapping of YAG and Ag1.5.

and 122 nm for Ag0.5, Ag1.0, Ag1.5 and Ag 2.0 respectively. The increase in particle size coexist with the lattice expansion.

3.1.2. Fourier transform Infrared Spectra (FT-IR)

FTIR spectra of YAG and doped samples are shown in figure 2. The peaks 3718-3433 cm^{-1} represents the vibrations of absorbed water H_2O which has O-H stretching vibrations [9]. The peaks from 2954 cm^{-1} to 2846 cm^{-1} represents the C-H (CH_2+CH_3) symmetrical and asymmetric stretching vibration [10]. The peaks at 1789 and 1435 cm^{-1} represents the COOH vibrations. The peaks at 800-400 cm^{-1} represents the metal oxygen [M-O] vibrations. Peaks at 763 cm^{-1} , 725 cm^{-1} , 692 cm^{-1}

are metal oxygen vibrations corresponds to Al-O, Y-O, Y-O-Al stretching [11].

3.2. Morphology and elemental composition

3.2.1. Scanning Electron Microscope (SEM)

The surface micrographs are shown in figure 3 for all the prepared samples. It is obvious that all the samples are showing tube like morphology [12]. The minimum crystallite size was observed in pristine YAG and the crystallite size is increasing with Ag doping. In addition to that the melting of edges is also seen in the Ag doped samples. This may be due to higher sintering temperature [13, 14]. The bright spots in the Ag doped samples are

owing to the presence of Ag. Elemental mapping was done in YAG and Ag1.5-YAG sample and the results are shown in figure 4 and Table 1. It shows that the atomic composition is in par with the calculates values of YAG and Ag1.5 obtained from elemental analysis.

3.3. Optical properties

3.3.1. Ultraviolet - Visible spectroscopy (UV-Vis)

Ultraviolet-visible spectroscopy refers to absorption spectroscopy or reflectance spectroscopy in part of the ultraviolet and visible regions of the electromagnetic spectrum. The absorption or reflectance in the visible range directly affects the apparent color of the chemicals involved. The electronic transition of atoms and molecules occur in this region of the spectrum.

The optical absorption spectra of the pure YAG and Ag doped YAG are shown in figure 5. The absorption peak in the visible range at 420 nm is

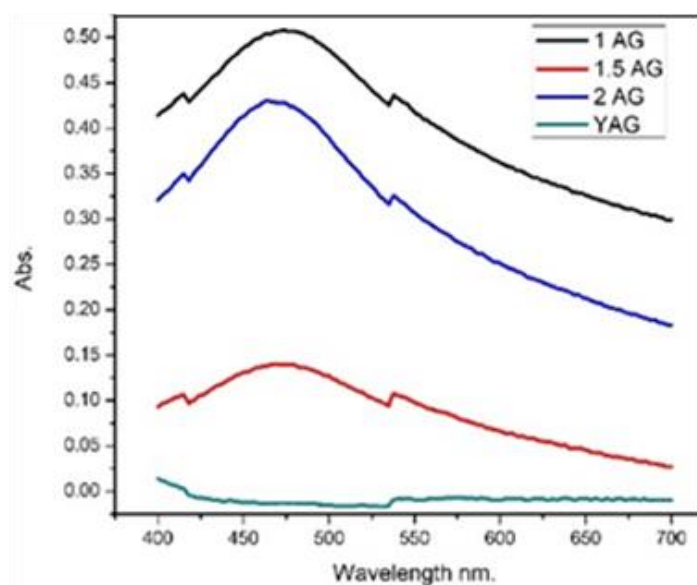


Figure 5. UV-Visible spectra of YAG and Ag doped YAG.

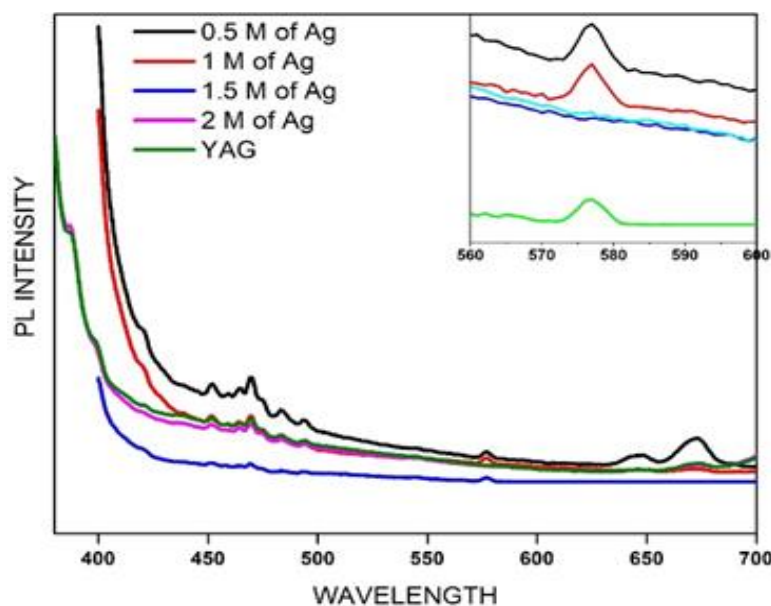


Figure 6. PL spectra of YAG and Ag doped YAG.

due to the incorporation of Ag in YAG matrix. The narrow gap between the valence and conduction band gives rise to surface plasmon resonance. The area under the absorption peaks increase as concentration of Ag in YAG increases. It can be seen that this peak exhibit blue shift [14]. On the other hand, the broad band absorption in the UV region of spectra can be attributed to the inter-band transition of electrons in silver nanoparticles [15].

3.3.2. Photoluminescence spectra (PL)

Photoluminescence spectroscopy is analytical technique that can determine quantities such as emission and excitation spectra and luminescence lifetimes. By this technique, a sample is excited by photons and the excess energy released by the sample through the emission of light can be detected and recorded for different modes, i.e., excitation, emission and luminescence decay lifetime. A spectrofluorometer is an instrument capable of recording the emission spectrum or both the excitation and emission spectra.

The PL spectra of YAG and Ag doped YAG nanophosphors are shown in figure 6. The luminescence properties of the pure and Ag-doped YAG samples were investigated and the excitation peak at 475 nm matches well with the blue light emitting properties [11]. Thus, it reveals that YAG sample can efficiently absorb the blue light. It is noted that the PL spectra were composed of one strong visible emission band positioned at about 578 nm in all the prepared YAG and Ag doped YAG nanophosphors. The strong peak observed at 578 nm in pure YAG and Ag0.5 and Ag1.0-YAG corresponds to green emission [16].

4. CONCLUSIONS

$Y_3Al_5O_{12}$ yttrium aluminium garnet nanophosphors and Ag doped YAG was prepared by Pechini method. The pure phase of YAG and cubic structure was confirmed from the XRD pattern. The peaks were indexed as per the JCPDS data. The sharp peak in the XRD reveals the good crystalline nature of the samples. Lattice expansion is indicated by the shift towards lower diffraction angle after the addition of Ag is also visible in the XRD pattern. The bending and stretching vibrations of the oxygen groups associated with YAG was observed in FTIR spectra. Tube like morphology

was noticed in the SEM and increase in crystallite size is also perceived after Ag was doped in YAG matrix. The melting of grain suggested that the sintering temperature is high. The elemental mapping confirmed the purity of synthesised samples and it in accordance with the calculated values. The absorption spectra at the range of 420 nm are obtained due to incorporation of Ag in YAG matrix. The PL spectra reveals the excitation peak at 475 nm which denotes the blue light emitting properties and the strong peaks at 578 nm in pure YAG and Ag0.5-YAG and Ag1.0-YAG that corresponds to green light emission hence proving its luminescence property.

ACKNOWLEDGMENTS

SSS and SK acknowledge the grant IUAC/XIII.7/UFR – 66306 received from Inter University Accelerator Centre, New Delhi, India for providing financial support.

REFERENCES

- [1] L. Yang, M. Chen, S. Yu, Z. Lv, S. Liu, Fabrication of YAG glass ceramic and its application for light emitting diodes, *13th International Conference on Electronic Packaging Technology & High-Density Packaging*, 1463-1466 (2012).
- [2] S. A. Hassanzadeh-Tabrizi, Synthesis and luminescence properties of YAG:Ce nanopowder prepared by the Pechini method. *Advanced Powder Technology*, **23**, 324-327 (2012).
- [3] N. Zhu, Y. Li, X. Yu, G. Wanyin, Synthesis and luminescent properties of YGG:Tb phosphors by Pechini method. *Journal of Luminescence*, **122**, 704-706 (2007).
- [4] V. Schiopu-Tucureanu, M. Alina, A. Avram, Synthesis and characterization of YAG:Ce phosphors for white LEDs. *Opto-Electronics Review*, **23**, 239-251 (2015).
- [5] M. Upasani, B. Butey, Doping effect of Mg on photoluminescence properties of YAG: Ce phosphor, *International Research Journal of Engineering and Technology* **2**, 2360-2363 (2015).
- [6] M. Harada, M. Goto, Synthesis of Y–Al–O compounds by a polymer complex method. *Journal of Alloys and Compounds* **408**, 1193-1195 (2006).
- [7] B. A. Smith, R. T. Dabestani, L. A. Lewis, C. V. Thompson, C. T. Collins, T. Aytug, Synthesis and Luminescence Characteristics of Cr³⁺ doped Y₃Al₅O₁₂ Phosphors; *Ph.D. Thesis, Oak Ridge National Laboratory, United States* (2015).
- [8] N. Iwashita, Chapter 2 - X-ray Powder Diffraction. In *Materials Science and Engineering of Carbon*, Eds: M. Inagaki, F. Kang. *Butterworth-Heinemann*, 7-25 (2016).
- [9] J. Kyzioł-Komosińska, C. Rosik-Dulewska, M. Pajak, I. Krzyżewska, A. Dzieniszewska, Adsorption of anionic dyes onto natural, thermally and chemically

- modified smectite clays. *Polish Journal of Chemical Technology* **16**, 33-40 (2014).
- [10] V. Schiopu-Tucureanu, M. Alina, I. Mihalache, M. Danila, M. Popescu, B. Bogdan, Synthesis and characterization of YAG:Ce,Gd and YAG:Ce,Gd/PMMA nanocomposites for optoelectronic applications. *Journal of Materials Science* **50** 1883-1890 (2015).
- [11] X. He, J. Liu, R. Li, B. Yang, K. Yu, M. Zeng, R. Yu, Effects of local structure of Ce³⁺ ions on luminescent properties of Y₃Al₅O₁₂: Ce nanoparticles. *Scientific Reports* **6**, 22238 (1)- 22238 (11) (2016).
- [12] A. Ehsani, H. Shiri, J. Shabani, Synthesis and highly efficient supercapacitor behavior of novel poly pyrrole / ceramic oxide nanocomposite film. *RSC Advances* **5**, 91062-91068 (2015).
- [13] L. Wang, F. Zhao, X. Yang, C.-Y. Pan, H. Huang, Property of YAG: Ce³⁺ nanophosphors prepared by solvothermal method using triethylene-tetramine as reaction solvent. *RSC Advances* **5**, 26339-26345 (2015).
- [14] L. Ptv, D. Priyanka, A. Arunachalam, Reduction of Silver Ions by Cell Free Extracts of *Westiellopsis* sp. *International Journal of Biomaterials* **6**, 1-6 (2015).
- [15] Halimah Mohamed. K, M. G. Naseri, A. R. Sadrolhosseini, A. Dehhangi, A. Kamalianfar, E. B. Saion, R. Zamiri, H. A. Ahangar, B. Y. Majlis, Silver Nanoparticle Fabrication by Laser Ablation in Polyvinyl Alcohol Solutions. *Chinese Physics Letters* **31**, 077803(1)- 077803(4) (2014).
- [16] S. R. Rosario, I. Kulandaisamy, K. D. A. Kumar, K. Ramesh, H. A. Ibrahim, N. S. Awwad, Ag-doped PbS thin films by nebulizer spray pyrolysis for solar cells. *International Journal of Energy Research* **44**, 4505-4515 (2020).

Antimony-lead melts for high temperature electrochemical applications

S.M. Mikhalev*, Paulo S.B. Julião, F.J.A. Loureiro, A.L. Shaula, D.P. Fagg

Centre of Mechanical Technology and Automation (TEMA), Department of Mechanical Engineering, University of Aveiro, 3810-193, Aveiro, Portugal

*Corresponding author, e-mail address: mikhalev@ua.pt

Received 15 October 2021; accepted 14 December 2021; published online 30 December 2021

ABSTRACT

The electrochemical behaviour of an antimony-lead melt upon saturation with oxygen was studied to assess further prospects of such melts as potential anode materials for high-temperature fuel cells.

A perovskite ceramic was used as a robust current collector material. The related mechanisms of alloying and phase segregation were revealed at different melt oxidation levels using combined impedance spectroscopy and thermodynamic analysis.

1. INTRODUCTION

Liquid metals have emerged as exciting potential materials for fuel cell and battery applications due to their suitable redox potentials and active participation in electrode reactions [1–3]. Mixtures of antimony and lead may be especially promising for these applications due to relatively low melting temperatures and low cost, together with redox

potentials that are compatible with the oxidation potential of most forms of carbon and also suitable for potential batteries [4-6].

Figure 1 presents a possible application of liquid Sb-Pb melt for plastic waste utilization in electricity production [7].

2. EXPERIMENTAL DETAILS

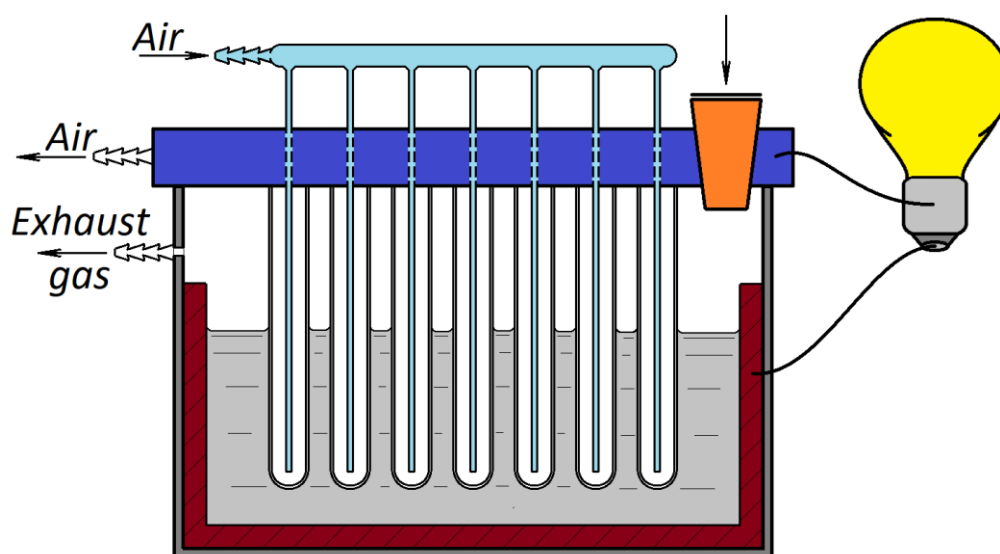


Figure 1. Principal scheme of plastic waste utilization reactor.

To investigate antimony-lead melts behavior in controlled conditions we made the following electrochemical cell. An yttria-stabilized zirconia tube was painted with platinum paste on the outer side to serve as an outer sensor electrode, allowing the oxygen activity in the melt to be determined. One YSZ disc covers the cell on the top and the other, used as oxygen pump, at the bottom.

Nevertheless, several problems were encountered with respect to the choice of current collector material. Platinum degrades in these conditions due to interreaction with the melt composition. Rhenium was also found to be unusable as it forms a volatile oxide at the working temperature of 700°C [8, 9].

To solve the problem, a perovskite ceramic disk of composition $(Y_{0.8}Ca_{0.2}Cr_{0.95}Ni_{0.05}O_{3\pm\delta})$ was, therefore, used [10]. This component is employed to function as both a current collector and as a potential probe for the melt. The corrosion stability of this ceramic was confirmed by long time tests of material in direct contact with antimony-lead melt at working temperature, followed by XRD analysis.

The entire volume of the YSZ cell was filled with previously mixed powders of antimony and lead (50/50% mol), corresponding to approximately 3.5 g of this mixture, with care taken due to prevent inhalation, due to the potential toxicity of the powder. The YSZ cell was then closed with top YSZ pellet and sealed with the help of a lower-temperature glass-ceramic sealant at 900 °C.

During the experiment oxygen was pumped inside the cell in portions equivalent to 200 Coulombs. After each step, the cell was completely disconnected from power supply and the sensor voltage was measured until its stabilization. This stable value was assumed to correspond to the attainment of equilibrium conditions between the melt and the oxygen amount introduced into the antimony-lead melt, as a function of the number of Coulombs passed.

The impedance spectra were recorded for each step, upon stabilization of the measured sensor potential in each case.

3. RESULTS AND DISCUSSION

Fig. 2 presents an example of the impedance response recorded for the antimony-lead melt, obtained at 700 °C at the oxidation degree of 97%. For clarity, the impedance corresponding to the offset on the real Z' axis (associated to the purely ohmic resistance) was subtracted. The impedance spectra show the existence of at least two semicircular responses in the measured frequency range.

The relaxation frequency of the low frequency term is shown to be strongly dependent on oxidation degree. This term reflects a diffusion process of oxygen exchange in the bulk volume of the melt. In contrast, relaxation frequency of the high frequency process is shown to be effectively independent of oxidation degree. This high frequency peak can be related to interfacial oxygen

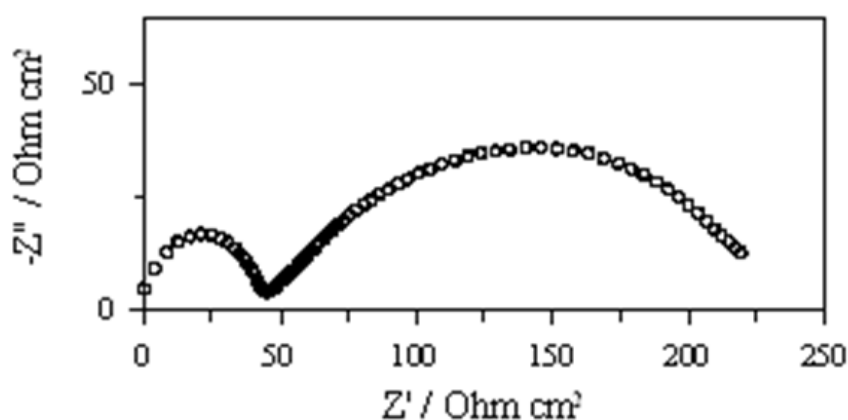


Figure 2. Impedance spectra of antimony-lead melt at 97 % oxidation degree.

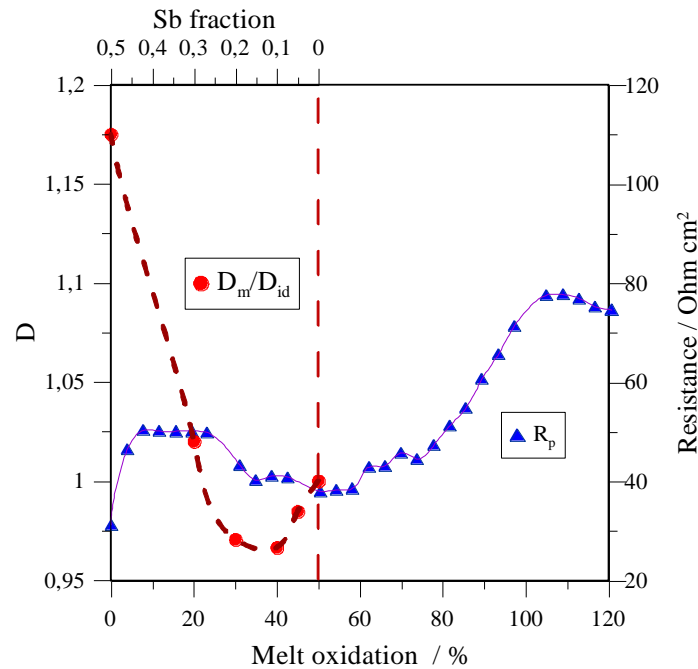


Figure 3. Polarization resistance values and degree of melt segregation

at various oxidation degrees. Horizontal line represents an ideal melt. The vertical line represents the total oxidation of Sb.

transfer from the zirconia pump to the metal mixture [11].

We have plotted impedance values vs oxidation degree in figure. 3. As antimony has a greater oxygen affinity than lead it can reduce any locally formed lead oxide to metallic lead. Therefore, during oxygen saturation, we firstly oxidize antimony metal from the mixture [12]. Therefore, we can replot this data as a function of the remaining antimony fraction in the melt.

Also, here we plot the degree of segregation of binary Sb-Pb alloy vs. antimony content, which as mentioned is also a function of oxidation degree (D_m/D_{id}). The degree of segregation reflects the level of reference to form melts with the same atoms as nearest neighbors and can be calculated from the available thermodynamic data [13, 14], where c_1 and c_2 are the concentrations of melt components, and $S_{cc}(0)$ is the long-wavelength limit of the concentration-concentration fluctuation:

$$D = \frac{c_1 c_2}{S_{cc}(0)} \quad (1)$$

A ratio greater than unity represents a compound forming liquid alloy formation, whereas values lower than unity reflect a segregated melt.

Upon oxidation, in the first stage of a compound forming melt, all characteristics shows almost constant behaviour as antimony metal is oxidised from a well distributed melt composition.

Later, as more antimony metal is oxidized, the melt composition passes into the segregation zone where lead and antimony separate in the melt composition. At this point, the lead falls to the bottom of the melt due to its higher density and is in contact with the pump surface. For this reason, the high frequency resistance, corresponding to interfacial transfer of oxygen from the pump surface to the melt, is shown to change. Moreover, at the bottom of the melt no antimony metal is now available to reduce the lead oxide and, hence, the lead oxide must diffuse upwards to meet the remaining antimony metal and be reduced. Consequently, the low frequency resistance also increases from this point, with an even greater increase shown once all antimony is oxidized, as observable by the variations in the total polarization resistance R_p in figure 3.

4. CONCLUSIONS

In conclusion, the current work forms a robust test equipment and technique for investigations of the

electrochemical behaviour of melts, which can allow the detailed study of different compositions of metal melt electrodes and their application in electrochemical devices. The development of such a method was shown to be critical due to the very aggressive environments present in this type of experiment.

The presented experiments also show the perspectives of using antimony-lead melt electrode for high temperature electrochemical cells and the importance of assessment of melt segregation on resultant electrochemical properties.

ACKNOWLEDGMENTS

This research was funded by the FCT (Fundação para a Ciência e a Tecnologia), grants numbers PTDC/CTM-CTM/2156/2020, PTDC/QUI-ELT/3681/2020, POCI-01-0247-FEDER-039926, POCI-01-0145-FEDER-032241, UIDB/00481/2020 and UIDP/00481/2020; and also, by Centro Portugal Regional Operational Programme (Centro2020), under the PORTUGAL 2020 Partnership Agreement, through the European Regional Development Fund (ERDF), grant number CENTRO-01-0145-FEDER-022083.

The authors acknowledge the support of national funds (OE), through FCT – Fundação para a Ciência e a Tecnologia, I.P., in the scope of the framework contract foreseen in the numbers 4, 5 and 6 of the article 23, of the Decree-Law 57/2016, of August 29, changed by Law 57/2017, of July 19.

Francisco J. A. Loureiro and Aliaksandr L. Shaula acknowledge FCT for the financial support with the references CEECIND/02797/2020 and CEECIND/01117/2020, respectively.

REFERENCES

- [1] A. Javadekar, A. Jayakumar, R.J. Gorte, J.M. Vohs, D.J. Buttrey, *J. Electrochem. Soc.* **158**, B1472–B1478 (2011).
- [2] W.A.G. McPhee, M. Boucher, J. Stuart, R.S. Parnas, M. Koslowske, T. Tao, B.A. Wilhite, *Energy & Fuel*, **23**, 5036–5041 (2009).
- [3] H. Abernathy, R. Gemmen, K. Gerdes, M. Koslowske, T. Tao, *J. Power Sources*, **196**, 4564–4572 (2011).
- [4] A. Javadekar, A. Jayakumar, R.J. Gorte, J.M. Vohs, D.J. Buttrey, *J. Electrochem. Soc.* **159**, A386–A389 (2012).
- [5] L. Otaegui, L.M. Rodriguez-Martinez, L. Wang, A. Laresgoiti, H. Tsukamoto, M.H. Han, C.-L. Tsai, I. Laresgoiti, C.M. López, T. Rojo, *J. Power Sources*, **247**, 749–755 (2014).
- [6] E. Edison, S. Sreejith, S. Madhavi, *ACS Appl. Mater. Interfaces*, **9**, 39399–39406 (2017).
- [7] H. Ju, S. Uhm, J.W. Kim, R.-H. Song, H. Choi, S.-H. Lee, J. Lee, *J. Power Sources*, **198**, 36–41 (2012).
- [8] C.W. Bale, E. Béllisle, P. Chartrand, S.A. Decterov, G. Eriksson, A.E. Gheribi, K. Hack, I.-H. Jung, Y.-B. Kang, J. Melançon, A.D. Pelton, S. Petersen, C. Robelin, J. Sangster, P. Spencer, M.-A. Van Ende, *Calphad*, **54**, 35–53 (2016).
- [9] H. Okamoto, *J. Phase Equilibria*, **13**, 580–581 (1992).
- [10] K.J. Yoon, C.N. Cramer, J.W. Stevenson, O.A. Marina, *J. Power Sources*, **195**, 7587–7593 (2010).
- [11] M.C.H. McKubre, D.D. Macdonald, *Measuring Techniques and Data Analysis, Impedance Spectrosc.* 129–204 (2005).
- [12] A. Jayakumar, S. Lee, A. Hornés, J.M. Vohs, R.J. Gorte, *J. Electrochem. Soc.* **157**, B365 (2010).
- [13] O. Akinlade, A.O. Boyo, B.R. Ijaluola, *J. Alloys Compd*, **290**, 191–196 (1999).
- [14] Y.P. Zaikov, P.A. Arkhipov, K.A. Plekhanov, V. V. Ashikhin, Y.R. Khalimullina, V. V. Chebykin, N.G. Molchanova, *Russ. J. Non-Ferrous Met*, **48**, 92–98 (2007).

Magnetic field, heat transfer and rheological analysis of a magnetorheometer using finite element method

Chandra Shekhar Maurya*, Chiranjit Sarkar

Department of Mechanical Engineering, Indian Institute of Technology, Patna, 801103, India

**Corresponding author, e-mail address: 1821me19@iitp.ac.in*

Received 19 October 2021; accepted 14 December 2021; published online 30 December 2021

ABSTRACT

Magnetorheological (MR) fluids show changes in apparent viscosity under an applied magnetic field. As a result, dramatic and reversible changes in rheological properties occurred, which permits many electromechanical devices to have potential utility in the aerospace, automobile, medical, and another field. Therefore, there is a need to investigate the rheological properties and heat developed due to changes in the rheological properties of MR fluids under the uniform magnetic field. This work presents the numerical simulation of magnetostatic, laminar fluid flow, and thermal field distribution of a plate-plate magnetorheometer using the finite element method. We analyzed the magnetic field distribution and magnitude of the magnetic field along the radius of the plates. We obtained a better uniform magnetic field along the radius of the plate with enhanced the magnitude of the magnetic field at a particular applied current compared to the other existing design of the rheometer. The maximum magnetic flux density at 4A of coil current is 1.3T. Laminar flow simulation gives the shear stress at the applied magnetic field as a function of the shear rate. We obtained the maximum velocity of the magnetic particles at the outer radius between plates. The heat generated due to the electromagnetic coil and slippage heating between the plates (i.e., MR region) is 302.5K and 308.5K at 3A current after 40 minutes of working time of magnetorheometer. The maximum temperature generated due to the combined effect of the electromagnetic coil and slippage is about 318K after 40 minutes of working time of magnetorheometer, much below the operating temperature of MR fluids. Here we enhanced the magnetic field density profile and magnitude of magnetic flux density along the working radius of the plate and minimized the effects of resistive coil heating in the MR fluid region by the coil and location design.

1. INTRODUCTION

Magneto-rheological fluids (MRF) are a suspension of iron particles in base oil (synthetic oil, water, etc.) that exhibit magnetic effects when a magnetic field is applied to it. When a magnetic field is applied to MRF, it causes significant and reversible changes in their rheological behavior [1][2]. MRFs generally act like Newtonian fluids (shear-thinning) in the absence of a magnetic field, but the relationship between shear stress and shear rate is balanced by yield stress in the presence of a magnetic field [3][4]. Yield stress depends on the increasing viscosity due to the formation of the chain-like structure of the magnetic

particles[5][6]. MR fluid is used in clutches, brakes, dampers, and actuators for transmission control, vibration control, and damping[7][8]. There are several magnetic, and heat transfer simulation works that were done on brakes and clutches, but few on the rheometer. Laun et al. (2008)[9] and Laun et al. (2010)[11] present the work on rheometer and obtained 0.74T and 1.37T at 3A of coil current respectively, but less work was performed on the heat transfer analysis of a rheometer. We provide a hybrid magnetorheometer model in this research that produces a magnetic flux of 1.3T at 4A along the whole working radius. We also go overheat

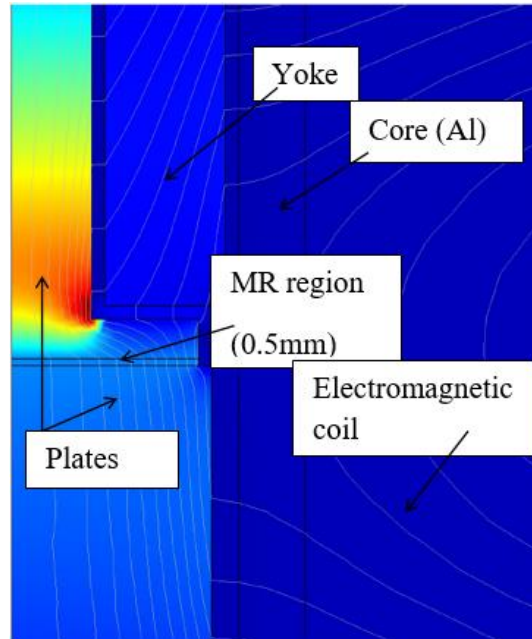


Figure 1. 2-D Axis symmetric magnetic field simulation of hybrid magnetorheometer.

creation from the electromagnetic coil's resistive heating and MR fluid slippage between the plates.

2. SIMULATION HYBRID MAGNETORHEOMETER

This research uses COMSOL's 2-D axisymmetric space to simplify the model and increase its accuracy. Figure 1 shows a 2-D axisymmetric schematic cross-section of the plate-plate magnetorheometer.

2.1. Magnetic Field Simulation

A "magnetic field" module in Comsol Multiphysics 5.3a software is used to simulate the magnetic field of the 2D axis-symmetric model. The magnetic field simulation is carried out using Ampere's Law, with the MUMPS solver and the air border acting as magnetic insulation. Except for the magnetic coil, Ampere's law applies to all border domains. The model is divided into two sections: solid and MR

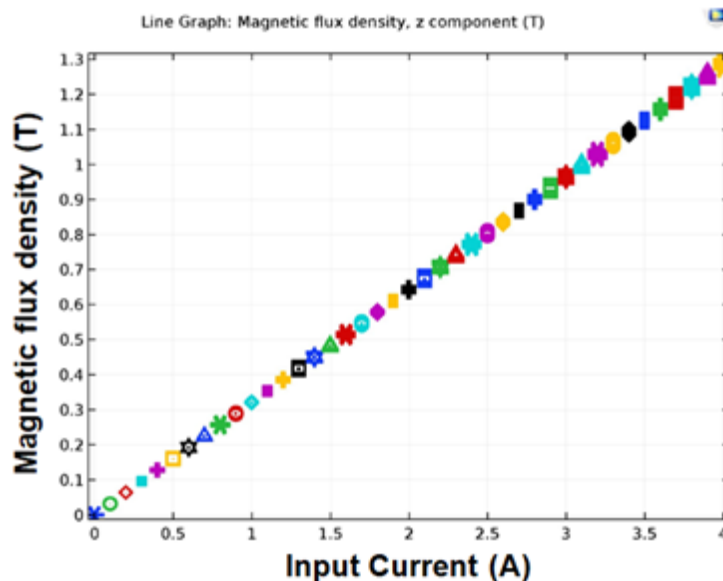


Figure 2. Magnetic flux density versus coil current at 0.5mm gap of MR region.

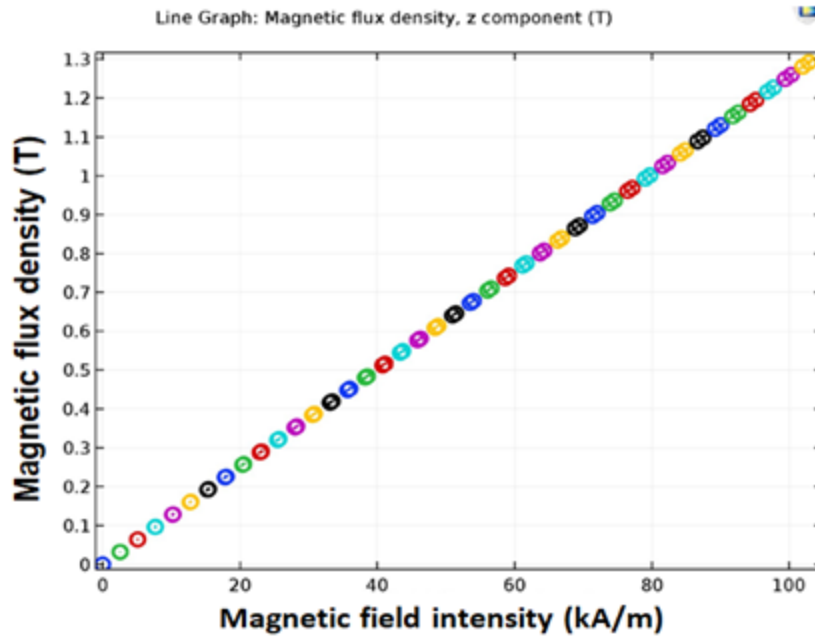


Figure 3. Variation of magnetic flux density versus magnetic flux intensity up to 4A input current.

fluid. The mesh size that was chosen was quite fine. The precision of the magnetic field is determined by the mesh quality of the MR region, which has a major impact on the simulation's computational outcomes. There are 2576 triangular elements and 399 geometric entity indices in this set. The plates and top yoke are made of low carbon steel 1010, which has a larger magnetic flux density than non-magnetic materials. The component materials are selected for their high relative permeability (μ_r) and low coercivity (H_c). The property, advantageous of low-coercivity material is this minimizes the remnant

field that is retained within the fixture upon removal of the magnetic field [12][13]. Components with low magnetic permeability that are not part of a magnetic circuit are generally chosen to reduce the magnetic leakage. MRF85, a self-prepared magnetorheological fluid made up of iron particles and silicone oil (viscosity 0.15 Pas) as base oil, was used in this simulation. The magnetic z-components of lines pass perpendicularly through the 0.5mm gap of sample space in Fig. 1, a 2-D axisymmetric simulation of the magnetic field of a hybrid magnetorheometer. The red zone in Fig 1 shows the maximum intensity of the magnetic field

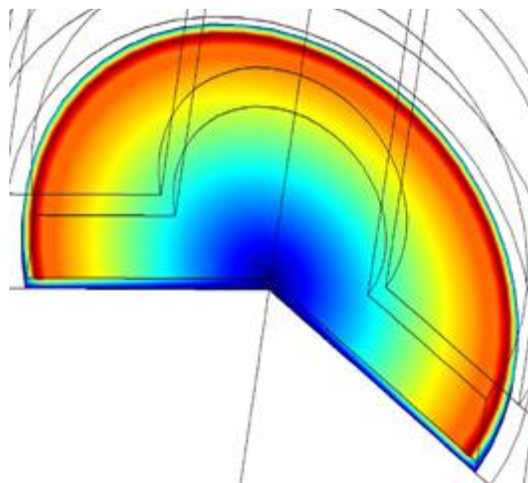


Figure 4. Distribution of velocity of MR fluid between the plates.

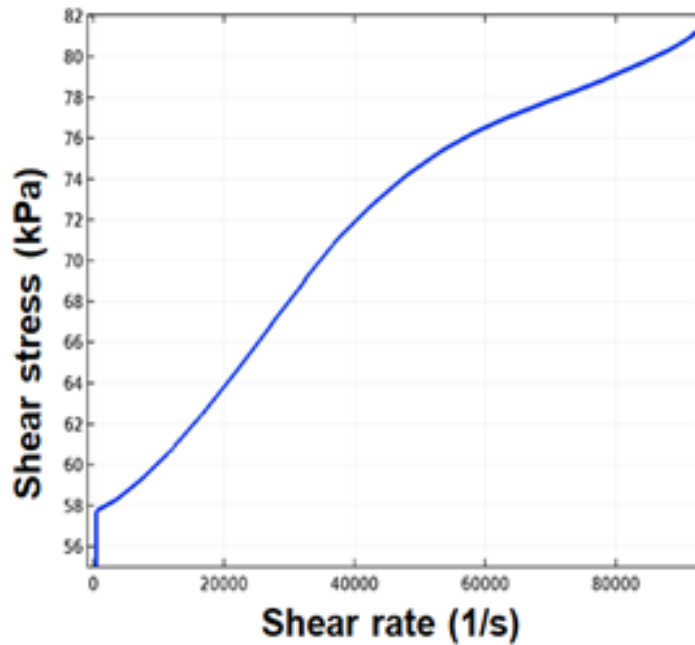


Figure 5. Variation of shear stress with shear rate.

in that area of plates. As the input current rises, the magnetic flux density rises to a certain point, after which the magnetic field begins to get saturated as the current rises. As demonstrated in Fig. 2, the highest magnetic flux density at 4A coil current is 1.3T. Figure 3 shows that the magnetic flux density

between parallel plates grows as the magnetic flux strength increases.

2.2. Laminar Flow Simulation

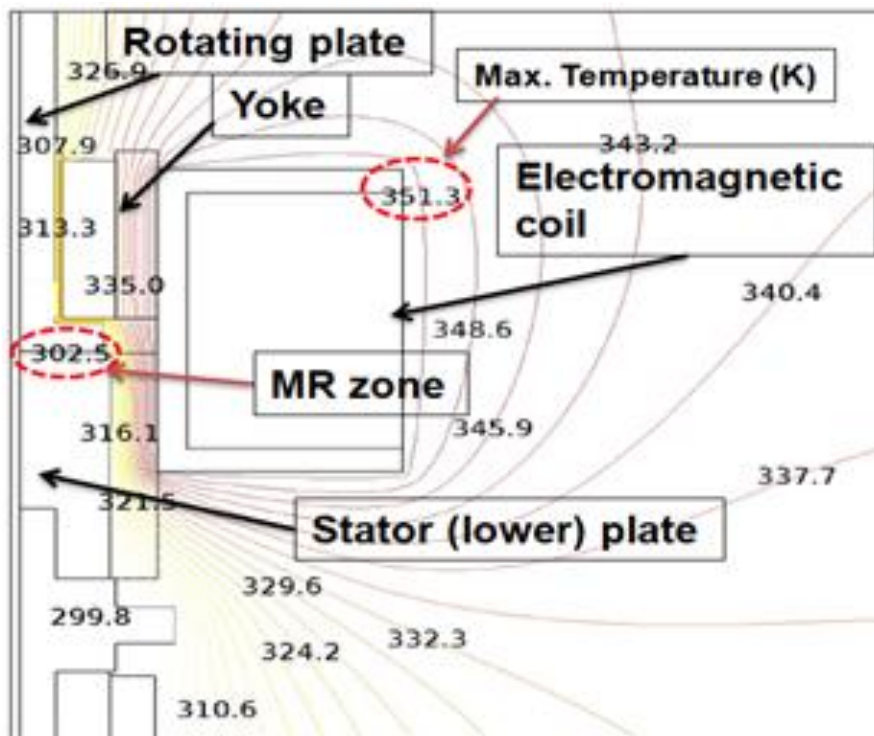


Figure 6. Distribution of temperature due to the resistive heating of the electromagnetic coil after 40 minutes of working time of magnetorheometer.

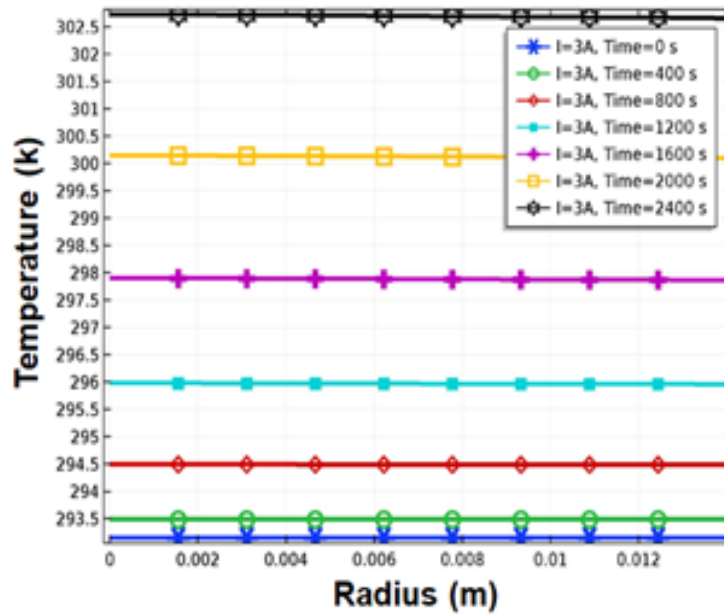


Figure 7. Variation of temperature through the radius of MRF region due to the resistive heating of the electromagnetic coil after 40 minutes of working time of magnetorheometer.

The shear stress at the applied magnetic field is calculated using laminar flow simulation and the shear stress impacts on shear stresses. MR fluid is placed between two parallel rotational plates with a 0.5mm gap between them, with the upper plate rotating while the lower plate remains fixed. The MR fluid particles rotate over stationary plates as the upper plates revolve. As shown in Fig. 4, the maximum velocity of MR fluid particles is away from the center of plates (the red zone area over the plates), which has an impact on MR particles collected away from the center. This can now be reduced by raising the magnetic flux density, because a strong chain forms among the particles under a high magnetic field, and the viscosity of the MR fluid rises. MRF85 yield stress is a function of magnetic flux density, with a value of 57.4KPa for 4A coil currents. An approximate polynomial equation was developed using Anton Paar MCR102, which shows the relation between magnetic flux intensity (B) and shear stress for MRF85, as shown in equation 1 [10].

$$\tau_y(kPa) = -603.78 \times B^4 + 1084.7 \times B^3 - 663.91 \times B^2 + 227.11 \times B + 2.5967 \quad (1)$$

Bingham model applied to describe post-yield behavior of MR fluid, while in the post-yield region a constant viscosity is assumed at a given

magnetic field. Bingham model equation is given below[6]:

$$\tau = \tau_y + \eta_0 \dot{\gamma} \quad (2)$$

Where τ is the shear stress, τ_y is the yield stress, $\dot{\gamma}$ is the shear rate, η_0 is the viscosity of base - dynamic viscosity (η) As in equation 3. The shear stress of MR fluid increases with increasing the shear rate, as shown in Fig. 5.

$$\eta \dot{\gamma} = \tau - \tau_y + \eta_0 \dot{\gamma} \quad (3)$$

2.3. Heat Transfer Simulation

The temperature is controlled by the hybrid magnetorheometer, which is generated primarily by two sources: (1) resistive heating of the electromagnetic coil, and (2) slippage of MR fluid between the plates. In regards to the physical working conditions, the simulation was performed for 40 minutes of working time of magnetorheometer, and the maximum temperature generated in the MR fluid zone as a result of the combined effects of resistive electromagnetic coil heating and slippage was approximately 318K.

2.3.2. Effect of Slippage

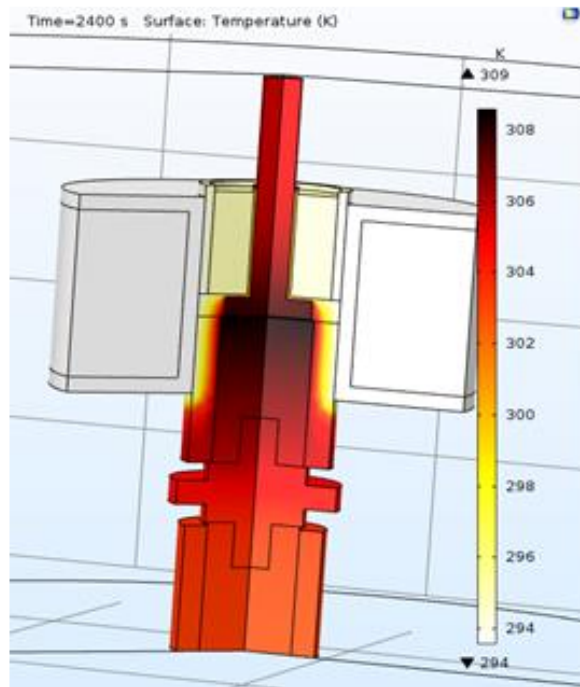


Figure 8. Distribution of temperature over the surface of rheometer due to slippage after 40 minutes of working time of magnetorheometer.

Due to the increased viscosity of MR fluid in the presence of the magnetic field, it becomes tough to break the chains when the rheometer plates begin to slip. The simulation is based on the idea that viscosity between the plates causes shear stress, which is then transformed into heat flow. The heat produced by slippage in the current magnetic field is more than the heat produced by slippage in the absence of a magnetic field. The temperature generated by MR fluid slippage in the presence of a magnetic field is 308.5K, which is higher than the temperature generated by the resistant coil. After 1 hour of working time of magnetorheometer, the maximum temperature generated is 313K, which is relatively low. As indicated in Fig. 8, the largest quantity of heat generated by slippage is near the MR sample. When compared to slippage heating, the temperature generated by resistive heating of the electromagnetic coil is lower. Slippage heating has a greater impact on the MR sample zone, thus we must keep it under control for the duration of the project. The maximum operating temperature limit of the MRF85 is 443k, which is significantly higher than the combined temperature impacts of the coil and slippage heating during 40 minutes of working time of magnetorheometer, as illustrated in Figs. 7 and 8.

4. CONCLUSIONS

The magnetic field over the MR sample was enhanced in this study; the magnetic flux density was 1.3T at 4A of input coil current. A homogeneous magnetic field is generated over the MR sample using this hybrid magnetorheometer model. Because the temperature created by the sum of electromagnetic coil heating and slippage heating is around 318K, which is well below the operating temperature of MR fluid, there is no requirement for water cooling for the 40 minutes of working time of magnetorheometer. Temperature variation is similarly constant around the radius, as seen in Figs. 7 and 8, and no temperature gradients occurred over the MR sample as a result. Now in this way, we improved the design of the magneto rheometer by enhancing the magnetic flux density and controlling the temperature over the MR sample.

ACKNOWLEDGMENTS

The authors would like to express their gratitude to the smart material and machines lab at the Department of Mechanical Engineering at IIT Patna, Patna, for supplying a rotational rheometer

(Anton Paar MCR102) and all other resources utilized in this study.

REFERENCES

- [1] D. Susan-Resiga, "A rheological model for magneto-rheological fluids," *J. Intell. Mater. Syst. Struct.*, vol. **20**, no. 8, pp. 1001–1010 (2009).
- [2] C. S. Maurya and C. Sarkar, "Effect of Fe₃O₄ Nanoparticles on Magnetorheological Properties of Flake-Shaped Carbonyl Iron Water-Based Suspension," *IEEE Trans. Magn.*, vol. **56**, no. 12, pp. 1–8 (2020).
- [3] C. S. Maurya and C. Sarkar, "Synthesis and characterization of novel flake-shaped carbonyl iron and water-based magnetorheological fluids using laponite and oleic acid with enhanced sedimentation stability," *J. Intell. Mater. Syst. Struct.*, vol. **32**, no. 14, pp. 1624–1639 (2021).
- [4] A. Farjoud, M. Ahmadian, N. Mahmoodi, X. Zhang, and M. Craft, "Nonlinear modeling and testing of magneto-rheological fluids in low shear rate squeezing flows," *Smart Mater. Struct.*, vol. **20**, no. 8, p. 14 (2011).
- [5] C. S. Maurya and C. Sarkar, "Rheological and creep and recovery behavior of carbonyl iron water-based magnetorheological gel using laponite as an additive and oleic acid as a surfactant," *Rheol. Acta*, vol. **51** (2021).
- [6] C. S. Maurya and C. Sarkar, "Rheological response of soft flake-shaped carbonyl iron water-based MR fluid containing iron nanopowder with hydrophilic carbon shell," *Rheol. Acta*, vol. **60**, no. 5, pp. 277–290 (2021).
- [7] C. S. Maurya and C. Sarkar, "Dynamic and creep and recovery performance of Fe₃O₄ nanoparticle and carbonyl iron microparticle water-based magnetorheological fluid," *J. Intell. Mater. Syst. Struct.* (2021).
- [8] J.D. Carlson and M.R. Jolly, "MR fluid, foam and elastomer devices," *Mechatronics*, vol. **10**, no. 4-5, p. 555-569. (2000).
- [9] H. M. Laun, G. Schmidt, C. Gabriel, and C. Kieburg, "Reliable plate-plate MRF magnetorheometry based on validated radial magnetic flux density profile simulations," *Rheol. Acta*, vol. **47**, no. 9, pp. 1049–1059 (2008).
- [10] H. M. Laun, C. Gabriel, and C. Kieburg, "Twin gap magnetorheometer using ferromagnetic steel plates—Performance and validation," *J. Rheol.*, vol. **54**, no. 2, pp. 327–354 (2010).
- [11] C. Gabriel and H. M. Laun, "Combined slit and plate-plate magnetorheometry of a magnetorheological fluid (MRF) and parameterization using the Casson model," *Rheol. Acta*, vol. **48**, no. 7, pp. 755–768. (2009).
- [12] C. S. Maurya and C. Sarkar, "Magnetic and Transient Temperature Field Simulation of Plate – Plate Magnetorheometer Using Finite-Element Method," *IEEE Trans. Magn.*, vol. **56**, no. 4, pp. 1–9 (2020).
- [13] M. Ocalan and G. H. McKinley, "High-flux magnetorheology at elevated temperatures," *Rheol. Acta*, vol. **52**, no. 7, pp. 623–641 (2013).

Nanomaterials Science & Engineering (NMS&E), Vol.3, No.2, 2021

NMS&E

**Department of Mechanical Engineering
University of Aveiro
Aveiro 3810-193
Portugal**

<https://proa.ua.pt/index.php/nmse/>

ISSN: 2184-7002